Detailed Complementary Consistency: Wave Function Tells Particle How to Hop, Particle Tells Wave Function How to Collapse

Lei Huang, *Zhecun Shi*, *and Linjun Wang**

Key Laboratory of Excited-State Materials of Zhejiang Province, Department of Chemistry, Zhejiang University, Hangzhou 310058, China

ABSTRACT: In mixed quantum-classical dynamics, the quantum subsystem can have both wave function and particle-like descriptions. However, they may yield inconsistent results for the expectation value of the same physical quantity. We here propose a novel detailed complementary consistency (DCC) method based on the principle of detailed internal consistency. Namely, wave function along each trajectory tells particle how to hop, while particle tells wave function how to collapse based on active states in the trajectory ensemble. As benchmarked in a diverse array of representative models with localized nonadiabatic couplings, DCC not only achieves fully consistent results (i.e., identical populations calculated based on wave functions and active states), but also closely reproduces the exact quantum results. Due to the high performance, our new DCC method has great potential to give a consistent and accurate mixed quantum-classical description of general nonadiabatic dynamics after further development.

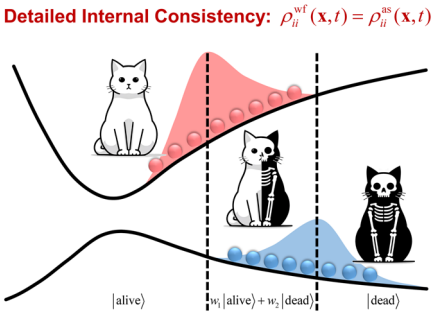

TOC Graphic

In chemistry, physics, biology, and materials science, many important processes (e.g., proton transfer,[1-3] charge transport,[4-6] exciton diffusion,[7-9] energy relaxation,[10-13] and singlet fission[14-17]) all belong to the category of nonadiabatic dynamics. Due to the presence of quantum transitions, the traditional Born-Oppenheimer approximation is no longer valid, and the electronic and nuclear dynamics become strongly coupled. To accurately simulate these nonadiabatic processes, different quantum dynamics methods have been proposed, including, for instance, the multiconfigurational time-dependent Hartree (MCTDH),[18,19] the time-dependent density matrix renormalization group (TD-DMRG),[20,21] and the hierarchical equations of motion (HEOM).[22-26] Despite the great successes, fully quantum dynamics generally needs high computational cost for large complex systems, which has significantly limited its applications.

Mixed quantum-classical dynamics has emerged as a promising alternative to fully quantum dynamics for studying complex nonadiabatic dynamics.[27,28] We may consider a general system with both electronic and nuclear degrees of freedom (DOFs), whose coordinates are **r** and **x**, respectively. In a mixed quantum-classical manner, the nuclei move classically, and the electron is propagated quantum mechanically along the nuclear trajectory. At each time t for each trajectory n, the nuclear coordinates are given by $\mathbf{x}^n(t)$ and the electronic wave function $\left|\psi^n(\mathbf{r},t)\right\rangle$ can be expressed as

$$\left|\psi^n(\mathbf{r},t)\right\rangle = \sum_i w_i^n(t)\left|\phi_i(\mathbf{r};\mathbf{x}^n(t))\right\rangle, \tag{1}$$

where $\left|\phi_i(\mathbf{r};\mathbf{x}^n(t))\right\rangle$ is the electronic basis for state i and $w_i^n(t)$ is the corresponding expansion coefficient. As a result, the wave function description of the population distribution on electronic state i at nuclear position **x** is given by[29]

$$\rho_{ii}^{\mathrm{wf}}(\mathbf{x},t)=\frac{1}{N}\sum_{n}\left|w_i^n(t)\right|^2\,\delta(\mathbf{x}-\mathbf{x}^n(t))\,, \tag{2}$$

where N is the number of trajectories. To give a particle-like description of the same distribution, we also assume that each trajectory n occupies an active electronic state $a_n(t)$ at each time t. Then, the population distribution can also be calculated by the probability that a trajectory stays at the specific position $\mathbf{x}$ and state i,[29]

$$\rho_{ii}^{\mathrm{as}}(\mathbf{x},t)=\frac{1}{N}\sum_{n}\delta_{i,a_n(t)}\delta(\mathbf{x}-\mathbf{x}^n(t))\,. \tag{3}$$

In principle, these two descriptions in Eqs. (2) and (3) should yield identical results at any time and any place because they represent different interpretations of the same population distribution. In the discussions below, this is referred to as the principle of detailed internal consistency of mixed quantum-classical dynamics.

As a seminal mixed quantum-classical dynamics method, Tully's fewest switches surface hopping (FSSH)[30] has been widely utilized in many research fields. The FSSH hopping probabilities are defined along each trajectory to ensure that the fraction of trajectories on each surface at any time follows the statistical populations based on wave functions. Although the FSSH results have shown good detailed balance,[31,32] the detailed internal consistency is not guaranteed due to the presence of frustrated hops and lack of decoherence.[33-37] Recently, we proposed the auxiliary branching corrected surface hopping (A-BCSH)[38] and the auxiliary branching corrected mean field (A-BCMF)[39] methods, which have achieved significantly better accuracy and consistency simultaneously compared to FSSH, implying a possible intrinsic connection between accuracy and detailed internal consistency in mixed quantum-classical dynamics.

When inconsistency arises, it is not straightforward to directly equate $\rho_{ii}^{\mathrm{wf}}(\mathbf{x},t)$ and $\rho_{ii}^{\mathrm{as}}(\mathbf{x},t)$ due to the ambiguity regarding the accuracy of these two distributions. To solve this problem, we apply the consistency correction in order. On one side, along each trajectory, the wave function propagated by the time-dependent Schrödinger equation (TDSE) could give the first-order derivative of population with respect to time and thus defines the population fluxes between electronic states. These population fluxes cannot be obtained from the particle-like description based on active states, in which the system moves classically on adiabatic surfaces. Thereby, it is natural to utilize these population fluxes to redistribute the occupation of active states, which ensures the unidirectional consistency from wave function to particle-like descriptions. Namely, wave function tells particle how to hop, just as in the traditional FSSH.[30] On the other side, for systems with localized nonadiabatic couplings (NACs), the occupation of active states generally gives a better description of the spatial distribution than the wave function by TDSE,[40,41] which may give erroneous populations for electronic states with too high energies. Thereby, we can use the distribution of active states to properly collapse the wave function and introduce decoherence. As a result, the detailed internal consistency can be realized for population distributions in both the nuclear phase space and the electronic state space. Note that the wave function collapse may significantly change the population fluxes, and thus should be made after the surface hops.

Based on the detailed internal consistency, we present a detailed complementary consistency (DCC) method. The total Hamiltonian of a general system is written as

$$\hat{H} = \hat{T}_n + \hat{H}_e(\mathbf{r};\mathbf{x}), \tag{4}$$

where $\hat{T}_n$ represents the kinetic energy operator of the nuclei, and $\hat{H}_e(\mathbf{r};\mathbf{x})$ is the electronic Hamiltonian at the given nuclear position $\mathbf{x}$. As in FSSH, we generate a series of trajectories. For each trajectory n, suppose the nuclear coordinates are $\mathbf{x}^n$ at time t. By solving the time-independent Schrödinger equation,

$$\hat{H}_e(\mathbf{r};\mathbf{x}^n)\left|\phi_i(\mathbf{r};\mathbf{x}^n)\right\rangle = E_i(\mathbf{x}^n)\left|\phi_i(\mathbf{r};\mathbf{x}^n)\right\rangle, \tag{5}$$

we can get all the adiabatic energies $\{E_i(\mathbf{x}^n)\}$ and the corresponding adiabatic states $\left\{\left|\phi_i(\mathbf{r};\mathbf{x}^n)\right\rangle\right\}$. The electronic wave function $\left|\psi^n(\mathbf{r})\right\rangle$ can be linearly expanded as

$$\left|\psi^n(\mathbf{r})\right\rangle = \sum_i w_i^n \left|\phi_i(\mathbf{r};\mathbf{x}^n)\right\rangle, \tag{6}$$

where $\{w_i^n\}$ are the expansion coefficients. Substituting Eq. (6) into the TDSE gives

$$i\hbar\frac{d}{dt}w_i^n = \sum_j w_j^n (V_{ij}^n - i\hbar\dot{\mathbf{x}}^n\cdot\mathbf{d}_{ij}^n), \tag{7}$$

where $V_{ij}^n = \left\langle\phi_i(\mathbf{r};\mathbf{x}^n)\,|\,\hat{H}_e(\mathbf{r};\mathbf{x}^n)\,|\,\phi_j(\mathbf{r};\mathbf{x}^n)\right\rangle$ are the matrix elements of the adiabatic Hamiltonian and $\mathbf{d}_{ij}^n = \left\langle\phi_i(\mathbf{r};\mathbf{x}^n)\,|\,\nabla_{\mathbf{x}}\phi_j(\mathbf{r};\mathbf{x}^n)\right\rangle$ are the NACs between adiabatic states i and j. The time evolution of the density matrix element $\rho_{ij}^{n,\mathrm{wf}} = w_i^n (w_j^n)^*$ along the trajectory is then given by[30]

$$i\hbar\frac{d}{dt}\rho_{ij}^{n,\mathrm{wf}} = \sum_k \left[\rho_{kj}^{n,\mathrm{wf}}(V_{ik}^n - i\hbar\dot{\mathbf{x}}^n\cdot\mathbf{d}_{ik}^n) - \rho_{ik}^{n,\mathrm{wf}}(V_{kj}^n - i\hbar\dot{\mathbf{x}}^n\cdot\mathbf{d}_{kj}^n)\right]. \tag{8}$$

The nuclei move on the active surface a through solving the Newtonian equation

$$\frac{d\mathbf{p}^n}{dt} = -\nabla_{\mathbf{x}}V_{aa}^n, \tag{9}$$

where $\mathbf{p}^n$ represents the nuclear momenta.

In principle, different approaches exist to ensure the consistency of active states according to the population fluxes. For instance, surface hopping probabilities can be defined based on NACs as in FSSH[30] and global fluxes as in the global flux surface

hopping (GFSH).[42] Recently, we have shown that both FSSH and GFSH with proper branching correction gives identical results in a large number of multilevel scattering problems.[43] In principle, this consistency correction can also be realized via coupled trajectories.[44,45] For simplicity, we here adopt the FSSH hopping probabilities and use velocity rescaling along the NAC direction to conserve the total energy for successful surface hops in each DCC trajectory.

For the consistency correction of wave functions based on active states at each time t, a step-by-step outline of the algorithm is as follows:

1. We estimate the local trajectory density for each trajectory. For trajectory n, suppose the nuclear coordinates and momenta are given by $\mathbf{x}^n(t)$ and $\mathbf{p}^n(t)$ at time t, respectively. We determine the number of local trajectory neighbors on each surface i whose positions are within a specified distance ε and directions of momenta are within a specified angular distance β by

$$N_i^n = \sum_{l=1}^{N} \Theta\left(\varepsilon^2 - \| \mathbf{x}^n - \mathbf{x}^l \|^2\right) \Theta\left(\frac{\mathbf{p}^n \cdot \mathbf{p}^l}{\| \mathbf{p}^n \| \cdot \| \mathbf{p}^l \|} - \cos(\beta)\right) \delta_{i,a_l} , \tag{10}$$

where a_l is the active state of trajectory l, $\| \cdot \|$ represents the Euclidean norm, and $\Theta(x)$ is the Heaviside step function defined as

$$\Theta(x) = \begin{cases} 1, & x \geq 0 \\ 0, & x < 0 \end{cases} \tag{11}$$

In principle, we should choose local trajectories with exactly the same momenta direction and the same position to estimate the local occupation number of active states. In practice, however, as a huge number of trajectories may be required. We here introduce the parameters ε and β to estimate the number of local trajectories for the

specified trajectory *n*, which could significantly enhance the numerical stability and efficiency. The convergence of DCC results with respect to ε and β is extensively studied and the results are given in the Supporting Information (SI). Given Eq. (10), the local trajectory density for the *n*-th trajectory is calculated as

$$\rho_{ii}^{n,\mathrm{as}} = \frac{N_i^n}{\sum_j N_j^n}, \tag{12}$$

which represents the local occupancy of active states on surface *i* close to trajectory *n*. We also calculate the population of each state *i* based on the wave function as

$$\rho_{ii}^{n,\mathrm{wf}} = \left| w_i^n \right|^2, \tag{13}$$

where w_i^n is the wave function coefficient of state *i* for trajectory *n*.

2. We determine whether inconsistency between $\{\rho_{ii}^{n,\mathrm{as}}\}$ and $\{\rho_{ii}^{n,\mathrm{wf}}\}$ for each trajectory *n* happens by hypothesis testing. In general, hypothesis testing determines whether the observed samples agree with a specific distribution, particularly when these samples fall outside the confidence region with reasonable confidence. In this study, the occupation of active states in the particle-like description can be regarded as a sample from the distribution characterized by the wave function description. For two-state systems, we can use z-test. According to the Born interpretation of wave function in quantum mechanics, the local occupation of the first adiabatic state can be treated as a sample from a binomial distribution with an expected value of $\mu_n = \rho_{11}^{n,\mathrm{wf}}$ and a standard deviation of $\sigma_n = [\rho_{11}^{n,\mathrm{wf}}(1-\rho_{11}^{n,\mathrm{wf}})]^{1/2}$. The z-score is calculated as

$$z_n = \frac{\left| \rho_{11}^{n,\mathrm{as}} - \rho_{11}^{n,\mathrm{wf}} \right|}{\sigma_n / \sqrt{\sum_l N_l^n}}. \tag{14}$$

Suppose the confidence region is described by a parameter *z*. If $z_n > z$, consistent

correction to the wave function should be carried out to ensure the detailed internal consistency. For general cases with M adiabatic states, we can use χ^2-test instead. Namely, we calculate the χ^2 statistic with $\{\rho_{ii}^{n,\mathrm{as}}\}$ and $\{\rho_{ii}^{n,\mathrm{wf}}\}$, and then compare it to the χ^2 distribution for M degrees of freedom to determine the corresponding p-value. If the p-value is less than the specified significance level η, there is inconsistency between the occupation of active states and the population calculated by wave functions.

3. If inconsistency is identified, the wave function should be properly collapsed. Because each trajectory in the trajectory ensemble has the corresponding wave function, there also exist many potential solutions to carry out consistency correction to the wave functions based on active states. We here consider the simplest approach. If $\rho_{ii}^{n,\mathrm{as}}$ is inconsistent with $\rho_{ii}^{n,\mathrm{wf}}$ for any state i in trajectory n, the wave function collapse is realized through resetting the diagonal elements of the density matrix as

$$\rho_{ii}^{n,\mathrm{wf}} = \rho_{ii}^{n,\mathrm{as}}, \tag{15}$$

At the same time, we rescale the off-diagonal density matrix elements by[29]

$$\rho_{ij}^{n,\mathrm{wf}} = \frac{\sqrt{\rho_{ii}^{n,\mathrm{as}}\rho_{jj}^{n,\mathrm{as}}}}{|\, w_i^n (w_j^n)^* \,|} w_i^n (w_j^n)^*. \tag{16}$$

The new density matrix is further used for the propagation of trajectory n by Eq. (8). As the calculation of $\rho_{ii}^{n,\mathrm{as}}$ relies on trajectories close to trajectory n, the trajectories in DCC simulations become coupled.

Note that the momenta direction considered in Eq. (10) bears some similarity to that used in the BCSH method.[53] However, the main idea of BCSH is that the wave function should be collapsed when wave packets are reflected, but DCC relies on the detailed internal consistency without assumption of the reflection criterion. As a

specified time, trajectories from different pathways may stay at the same position. To distinguish the different pathways, it is a natural choice to pick out trajectories with similar directions to get the local trajectory density. As far as consistency is maintained for each pathway, we can ensure the detailed internal consistency for the whole system.

To extensively benchmark the performance of DCC, we study a variety of models proposed in the literature and use the FSSH[30] results and the exact quantum dynamics by the discrete variable representation (DVR)[46-48] or the multi-layer MCTDH (ML-MCTDH)[19] as references. Atomic units are used unless otherwise noted. We first focus on the three standard one-dimensional scattering models proposed by Tully,[30] including the simple avoided crossing (SAC), the dual avoided crossing (DAC), the extended coupling with reflection (ECR) models. We then study two more challenging two-dimensional scattering models proposed by Subotnik,[49,50] i.e., the STD-1 and STD-2 models. We also consider three one-dimensional bound-state models designed by Agostini,[51,52] i.e., the BS-1, BS-2 and BS-3 models. Finally, we examine the performance of DCC in a photodissociation model proposed by Miller[54] and a three-mode pyrazine model proposed by Schneider and Domcke.[55,56] To facilitate the discussions about detailed internal consistency below, the DCC (FSSH) results based on wave functions and active states are named as DCC-wf and DCC-as (FSSH-wf and FSSH-as), respectively.

In Figure 1A, we show the transmission probability on the upper surface as a function of the initial momentum k in the SAC model. While FSSH-as properly characterizes the dynamics, FSSH-wf does not perform well for $k < 10$. In these low-

energy cases, many trajectories do not have enough kinetic energies to hop to the upper surface in the interacting region, leading to frustrated hops and inconsistency between active states and wave functions. As these trajectories leave the interacting region, the wave function propagated by TDSE still contributes to transmission on the upper surface, while the active states do not have such probabilities. Due to the inherent detailed internal consistency, DCC naturally solves this problem. Regardless of the analysis method, both DCC-as and DCC-wf reproduce the exact quantum dynamics for all the investigated k cases. Figure 1B shows strong Steuckelberg oscillations in the transmission on the upper surface in the DAC model due to quantum interference.[30] Compared with the exact quantum results, FSSH shows smaller oscillation amplitudes and different phases. Again, FSSH-as and FSSH-wf give inconsistent results for small k, similar to those in the SAC model. In comparison, DCC-as and DCC-wf with the phase correction[50] give fully consistent and much more accurate results.

In Figures 1C and 1D, we show probabilities of reflection on the lower surface and transmission on the upper surface in the ECR model, respectively. It is apparent that FSSH shows even more significant inconsistency in the small k cases. Both FSSH-as and FSSH-wf show evident oscillations and overestimated strengths in the reflection probabilities on the lower surface for $k < 14$ (see Figure 1C). The inconsistency of FSSH results in wrong population fluxes when the trajectories re-enter the interaction region. As shown in Figure 1D, FSSH-as gives no transmission on the upper surface for $k < 25$ because the kinetic energies are not enough to afford the surface hops, but FSSH-wf gives completely wrong results due to overcoherence. In comparison, DCC always

maintains the consistency and ensures accurate fluxes even when the wave packet experiences multiple interaction regions. These results highlight the importance of maintaining consistency in mixed quantum-classical simulations of complex systems.

Besides the final channel populations, we also examine the spatial distribution of population at different time to further benchmark the performance of DCC. As an illustration, we consider the ECR model with $k = 10$. Figure 2 shows three critical time snapshots of the dynamics, i.e., entry of the initial wave packet into the interaction region, reflection of the wave packet on the upper surface, and reentry of the reflected wave packet into the interaction region. Due to the nearly degenerate adiabatic surfaces in the interaction region, both FSSH and DCC achieve consistent results and the spatial distributions of population agree well with the exact quantum dynamics at the first snapshot (see Figures 2A and 2D). When the wave packets exit the interaction region and branch on different surfaces, however, inconsistency emerges between FSSH-wf and FSSH-as results (see Figures 2B and 2E). In particular, FSSH-wf underestimates (overestimates) the population of the upper (lower) state for $x < -1.5$, and it is the opposite for $x > 1.5$. As shown in Figures 2C and 2F, when the wave packets reenter the interaction region, the inconsistency of FSSH results in inaccurate transitions and too large (small) populations on the lower (upper) surface. Encouragingly, DCC reproduces the correct spatial distribution of population throughout the whole dynamics.

In the one-dimensional scattering models studied above, DCC has demonstrated consistency and high accuracy simultaneously. We further investigate whether the DCC method can effectively describe more complex problems involving more classical

DOFs. We consider two representative models proposed by Subotnik.[49,50] For the STD-1 model, the Hamiltonian is defined as[49]

$$H_{11}(x,y) = -A_1 \tanh(B_1 x), \tag{17}$$

$$H_{22}(x,y) = A_2 \tanh[B_2(x-1) + C_2 \cos(D_2 y + \pi/2)] + 3A_2/4, \tag{18}$$

$$H_{12}(x,y) = H_{21}(x,y) = A_3 \exp(-B_3 x^2), \tag{19}$$

where A_1 = 0.05, B_1 = 0.6, A_2 = 0.2, B_2 = 0.6, C_2 = 2.0, D_2 = 0.3, A_3 = 0.015 and B_3 = 0.3. To assess the performance of our DCC method across a broad range of parameters, we place the initial Gaussian wave packet on either the lower or the upper surface at (x_0, y_0), where x_0 = -4 and y_0 takes values of -2, -1, 0, 1, 2, 3, 4 or 5. In addition, the initial momentum is oriented at an angle θ of 0°, 15°, 30° or 45° with respect to the x-axis. When the initial wave packet is placed on the lower (upper) surface, the momenta range from 16 to 28 (8 to 20). In total, we have considered 832 initial conditions. We use a time step of dt = 0.2. For each set of initial parameters, the maximum simulation time for the dynamics corresponds to the time at which the electronic population passing through the boundaries (x = -15 or 25, y = -15 or 25) reaches 10^{-6} in the exact quantum dynamics. The entire space is divided by the two central lines (i.e., x = 5 and y = 5) into four subspaces, resulting in a total number of eight channels on the two surfaces. The population of each channel is calculated by integrating the electronic population density within the corresponding subspace.

To provide a comprehensive measure of the overall accuracy of FSSH and DCC methods in predicting channel populations for the large range of initial conditions, we define the root mean square error (RMSE) of population as

$$\mathrm{RMSE} = \sqrt{\frac{1}{8M}\sum_{j=1}^{M}\sum_{i=1}^{8}\left(P_i^{\mathrm{method},j} - P_i^{\mathrm{DVR},j}\right)^2}\,, \tag{20}$$

where M represents the number of total initial conditions, $P_i^{\mathrm{method},j}$ and $P_i^{\mathrm{DVR},j}$ are the populations of the i-th channel at the final snapshot for the j-th initial condition by a mixed quantum-classical dynamics method (i.e., FSSH or DCC) and the exact quantum dynamics with DVR,[46-48] respectively.

In Figures 3A and 3B, we show the RMSE of population for FSSH and DCC results. It is apparent that there exist notable differences between FSSH-wf and FSSH-as with values of about 0.09 at large k, indicating a considerable inconsistency in FSSH. Even when using the active states for trajectory analysis, the error of FSSH-as remains at about 0.03. These results imply the similar challenges identified in Figure 1C for the ECR model. Namely, after the wave packet encounters steep barriers, the active states and wave functions become inconsistent, primarily due to frustrated hopping and wave packet branching.[43,53] The cumulative errors become apparent when the wave packet reenters the interaction region. Encouragingly, DCC is free from these complications by holding the detailed internal consistency, significantly reducing the errors to about 0.01. As expected, both DCC-wf and DCC-as produce identical results.

The Hamiltonian of the STD-2 model is defined as[50]

$$H_{11}(x,y) = -E_0\,, \tag{21}$$

$$H_{22}(x,y) = -A\exp\left(-B(0.75(x+y)^2 + 0.25(x-y)^2)\right), \tag{22}$$

$$H_{12}(x,y) = H_{21}(x,y) = C\exp\left(-D(0.25(x+y)^2 + 0.75(x-y)^2)\right), \tag{23}$$

where A = 0.15, B = 0.14, C = 0.015, D = 0.06, and E_0 = 0.05. To conduct a thorough benchmark, we set the initial conditions with x_0 = -8 and y_0 in the range from -4 to 1,

and the angle θ with respect to the x-axis taking values of 0°, 15° or 30°. When starting from the upper (lower) surface, the momenta of the initial wave packet range from 8 to 20 (4 to 16). As a result, we analyze the channel populations over a set of 468 initial conditions. The time step size is set as dt = 0.2. Both x and y are in the range of (-15, 15). The entire space is divided by the two central lines (i.e., x = 0 and y = 0) into four subspaces, and the definition of channel populations is similar to that in STD-1.

As shown in Figures 3C and 3D, FSSH-wf and FSSH-as still produce inconsistent results. Compared with the STD-1 model, although the differences between FSSH-wf and FSSH-as results are smaller in the STD-2 model, the errors FSSH-as are increased, implying that small inconsistency during the nonadiabatic dynamics may induce large errors. In contrast, DCC-wf and DCC-as yield identical results and substantially reduce the errors to about 0.01, which are similar to those in STD-1. These results further suggest that ensuring the detailed internal consistency can significantly reduce the errors inherent in FSSH. Detailed results for the STD-1 and STD-2 models are given in the SI. In almost all initial conditions, DCC performs much better than FSSH, indicating a systemic improvement of accuracy for nonadiabatic dynamics simulations.

We further select a representative initial condition for the STD-2 model, where the initial wave packet starts from the excited surface with the initial parameters of x = -8, y = 0, θ = 15° and k = 16. In Figures 4A and 4D, we show the population distributions by DVR at the final snapshot (i.e., t = 1900 au) on the upper and lower surfaces, respectively. As the initial wave packet enters the interaction region from the left side, a new wave packet component is generated on the upper surface due to the strong NAC.

These two wave packet components branch in the interaction region. While the initial wave packet remains in this region, it spawns another wave packet component on the lower surface. However, because the NAC is weak at the edge of the interaction region, the intensity of the new wave packet component is relatively weak. Finally, the wave packets are completely separated, resulting in two primary population channels and a secondary population channel (see Figures 4A and 4D). As shown in Figures 4B and 4E, the population distribution of FSSH-wf even shows wrong numbers of wave packet components on both upper and lower surfaces due to the lack of decoherence. In contrast, DCC successfully reproduces both the shape and intensity of the exact quantum dynamics, demonstrating the accuracy of DCC in handling branching within the interaction region.

To further examine the potential of DCC in condensed-phase applications, we consider a one-dimensional bound-state model, which consists of one nuclear DOF and two electronic states. The Hamiltonian reads[51,52]

$$H_{11}(x) = \frac{1}{2}K(x - R_1)^2, \tag{24}$$

$$H_{22}(x) = \frac{1}{2}K(x - R_2)^2 + \Delta, \tag{25}$$

$$H_{12}(x) = H_{21}(x) = b\exp\left(-a(x - R_3)^2\right), \tag{26}$$

where $K = 0.02$, $a = 3.0$, $R_1 = 6.0$ and $R_2 = 2.0$. Considering different energy differences Δ and reorganization energies $E_r = K(R_1 - R_2)^2 / 2$, BS-1 and BS-3 are in the direct regime and BS-2 is in the inverted regime as in the Marcus theory of charge transfer.[57] The other parameters are listed in the SI. In BS-1 and BS-2, the initial wave packets are fully promoted to the excited state (S_1). In BS-3, 20% of the population is vertically

placed on the excited state creating a coherent superposition.

The time-dependent excited-state populations based on active states and wave functions can be respectively calculated as

$$\rho_{22}^{\mathrm{as}}(t)=\frac{1}{N}\sum_{n}\delta_{2,a_n(t)}\,, \tag{27}$$

$$\rho_{22}^{\mathrm{wf}}(t)=\frac{1}{N}\sum_{n}\left|w_2^n(t)\right|^2\,, \tag{28}$$

where $w_2^n(t)$ is the wave function component of the excited state at time t for the n-th trajectory. With the population distributions in Eq. (2), the indicator of coherence can be defined as[51]

$$\sigma_{12}(t)=\int \mathrm{d}\mathbf{x}\,\frac{\rho_{11}^{\mathrm{wf}}(\mathbf{x},t)\rho_{22}^{\mathrm{wf}}(\mathbf{x},t)}{\rho_{11}^{\mathrm{wf}}(\mathbf{x},t)+\rho_{22}^{\mathrm{wf}}(\mathbf{x},t)}\,, \tag{29}$$

which corresponds to the intensity of overlap between wave packets on the two surfaces.

As shown in Figure 5, because the nuclear wave packet periodically propagates through the crossing region, the excited-state population in the exact quantum dynamics experiences stepwise transitions to the ground state. And the coherence shows periodic increase and subsequent decay to zero due to the reflection and separation of wave packets on different surfaces. In all the three investigated bound-state models under different parameters and initial conditions, DCC-wf and DCC-as show accurate and consistent results, while both FSSH-wf and FSSH-as yield significant deviations. In the BS-3 model, the excited-state population of FSSH-wf even erroneously increases with time, which is the opposite of that in the exact quantum dynamics (see Figure 5E). In addition, FSSH-as strongly overestimates the population transfer from the excited state to the ground state due to the lack of decoherence (see Figure 5E). The shortcomings

of FSSH become more pronounced when the inconsistent wave function is used to calculate coherence. As shown in Figures 5B, 5D and 5F, FSSH remains overcoherent after the wave packet leaves the crossing region for the first time. In comparison, DCC perfectly captures the decoherence in the exact quantum dynamics. It is important to note that Agostini and coworkers have extensively studied the BS-3 model with many different methods,[52] none of which could reproduce the strong coherence peak at about t = 100 fs (see Figure 5F). In our present study, the DCC results are almost on top of the exact solutions, further highlighting the excellent performance of DCC.

To evaluate the performance of the DCC method in photoexcitation dynamics, we consider two additional models, i.e., a photodissociation model[54] and the three-mode pyrazine model.[55,56] In these cases, we study the populations of diabatic states, which are defined based on the wave function as[41]

$$\rho_{ii}^{\mathrm{dia,wf}}(t) = \frac{1}{N}\sum_{n}\left|c_i^n(t)\right|^2, \tag{30}$$

where $c_i^n(t)$ is the expansion coefficient of diabatic state i for the wave function at time t along trajectory n.

The photodissociation model contains one nuclear degree of freedom and three electronic states. The Hamiltonian elements are expressed as[54]

$$H_{ii}(x) = D_i\left(1-e^{-\beta_i(x-R_i)}\right)^2 + C_i, \tag{31}$$

$$H_{ij}(x) = A_{ij}e^{-a_{ij}(x-R_{ij})^2}, \tag{32}$$

where D_1 = 0.003, D_2 = 0.004, D_3 = 0.003, β_1 = 0.65, β_2 = 0.6, β_3 = 0.65, R_1 = 5.0, R_2 = 4.0, R_3 = 6.0, C_1 = 0.00, C_2 = 0.01, C_3 = 0.006, A_{12} = A_{23} = 0.002, A_{13} = 0, a_{12} = a_{23} = 16.0, R_{12} = 3.40, and R_{23} = 4.80. At time zero, the system is excited to the first diabatic

state from the harmonic ground state with the vibrational frequency ω = 0.005 and the equilibrium bond length x_e = 2.9. The nuclear mass is set as m = 20000.

In Figure 6A, we show the electronic populations of all the three diabatic states calculated by FSSH and DCC. The first population transfer process occurs between state 2 and the initially populated state 1 at about 10 fs, and there is a second population transfer between state 2 and state 3 at about 40 fs. Although the FSSH method gives correct description for the first population transfer, there are evident deviations when the wave packet enters the second interacting region. In contrast, the DCC method gives almost quantitative agreement with the quantum evolution of electronic populations, indicating that DCC can be used in multi-level systems with Morse potentials.

The two-level three-mode pyrazine model is more challenging. The relevant parameters were fitted from semi-empirical electronic structure calculations.[55] The Hamiltonian reads

$$\begin{aligned}\hat{H} = &\begin{bmatrix} E_1 & 0 \\ 0 & E_2 \end{bmatrix} + \sum_{i=10a,6a,1} \frac{\omega_i}{2}\left(\hat{P}_i^2 + \hat{R}_i^2\right)\begin{bmatrix} 1 & 0 \\ 0 & 1 \end{bmatrix} \\ &+ \begin{bmatrix} 0 & \lambda \\ \lambda & 0 \end{bmatrix}\hat{R}_{10a} + \begin{bmatrix} \kappa_{6a}^{(1)} & 0 \\ 0 & \kappa_{6a}^{(2)} \end{bmatrix}\hat{R}_{6a} + \begin{bmatrix} \kappa_1^{(1)} & 0 \\ 0 & \kappa_1^{(2)} \end{bmatrix}\hat{R}_1,\end{aligned} \tag{33}$$

where E_1 = 3.94 eV, E_2 = 4.84 eV, ω_{10a} = 0.118 eV, ω_{6a} = 0.074 eV, ω_1 = 0.126 eV, λ = 0.262 eV, $\kappa_{6a}^{(1)}$ = -0.105 eV, $\kappa_{6a}^{(2)}$ = 0.149 eV, $\kappa_1^{(1)}$ = 0.037 eV, and $\kappa_1^{(2)}$ = -0.254 eV. Here, $\{\hat{R}_i\}$ and $\{\hat{P}_i\}$ are coordinate and momentum operators for the three selected normal modes (i.e., 10a, 6a and 1). The width of the initial wave packet is set as that of the vibronic ground state and the second electronic state is occupied at time zero.

In Figure 6B, we show the time-dependent population of diabatic state 2 obtained by FSSH, DCC and ML-MCTDH. It is evident that FSSH performs poorly for the long-

time dynamics and gives the wrong equilibrium limit. In comparison, DCC performs much better and shows the correct oscillation phases and amplitudes during the whole population transfer process despite some deviations. A detailed examination of the convergence of DCC results with respect to the relevant parameters is given in the SI. We may find that the DCC results in the pyrazine model is insensitive to the choices of ε and β. Thereby, for some high-dimensional bound-state systems with localized NACs, we might be able to choose large ε and small $\cos(\beta)$ or even consider all the trajectories as neighbors for the consistency correction of wave functions based on active states.

In summary, we have presented the principle of detailed internal consistency for mixed quantum-classical nonadiabatic dynamics simulations. Namely, the population distributions based on wave functions and active states should be identical at any time and any space. Based on this principle, we have proposed a novel DCC method, which naturally involves surface hopping based on the wave function in individual trajectories and wave function collapse (i.e., decoherence) based on the local occupation of active states with neighboring trajectories. DCC has been extensively benchmarked across a series of representative models with localized NACs because the active states in these cases are well defined and can guide the wave function collapse. Both scattering and bound-state systems with different dimensions have been studied. In all investigated cases, DCC has exhibited high accuracy, regardless of using active states or wave functions for trajectory analysis. Due to the remarkable performance, the framework of DCC has presented significant potential for the application in general complex systems. From some point of view, our DCC method can also be regarded as a self-consistent

wave-particle description of the quantum subsystem in contact with a classical bath and deserves further study.

Finally, there are still a few points worth discussing. (1) Note that the DCC method is different from the consistent construction (CC) method developed recently.[29] Though both of the two methods take advantages of the occupation of active states, CC is a post-processing method to analyze the distribution of population and coherence after surface hopping simulations have been finished, but DCC is an on-the-fly nonadiabatic dynamics method that iteratively uses active states for wave function collapse and uses the modified wave function to guide surface hops along the trajectories. As a result, the trajectories in CC and DCC can be completely different. (2) For clarity, we here adopt the simplest algorithm to ensure the principle of detailed internal consistency. Namely, for a specified trajectory, the population of each state follows the local occupation of active states in the trajectory ensemble. We have shown that even such a local trajectory density approximation could give encouraging results. In principle, better solutions are possible. For instance, we may consider the spatial gradient or higher-order derivatives of the trajectory density to include non-local effects. (3) In the present study, we focus on illustration of maintaining the importance of detailed internal consistency in mixed quantum-classical dynamics. For systems with too many nuclear degrees of freedom, however, a limited number of trajectories may become too sparse and estimation of the local trajectory density may become difficult. As a result, the number of trajectories needed for DCC simulations with the current algorithm may increase significantly with the spatial dimensionality in some systems. To consider the principle of detailed internal

consistency for more complex condensed-phase systems (e.g., the Fenna-Matthews-Olson complex,[58] the spin-boson models,[59-62] and the Holstein-Peierls models[63-65]), more efficient algorithms are still needed to reduce the computational cost. These studies are currently under way.

AUTHOR INFORMATION

Corresponding Author

*Email: ljwang@zju.edu.cn

ORCID

Linjun Wang: 0000-0002-6169-7687

Author Contributions

The manuscript was written through contributions of all authors. All authors have given approval to the final version of the manuscript.

Notes

The authors declare no competing financial interests.

ACKNOWLEDGMENTS

L.W. acknowledges support from the National Natural Science Foundation of China (Grant No. 22273082) and the High-Performance Computing Center in Department of Chemistry, Zhejiang University.

ASSOCIATED CONTENT

Supporting Information

We give the computational details, convergence of the DCC results, and additional

results for the two-dimensional models.

This information is available free of charge online.

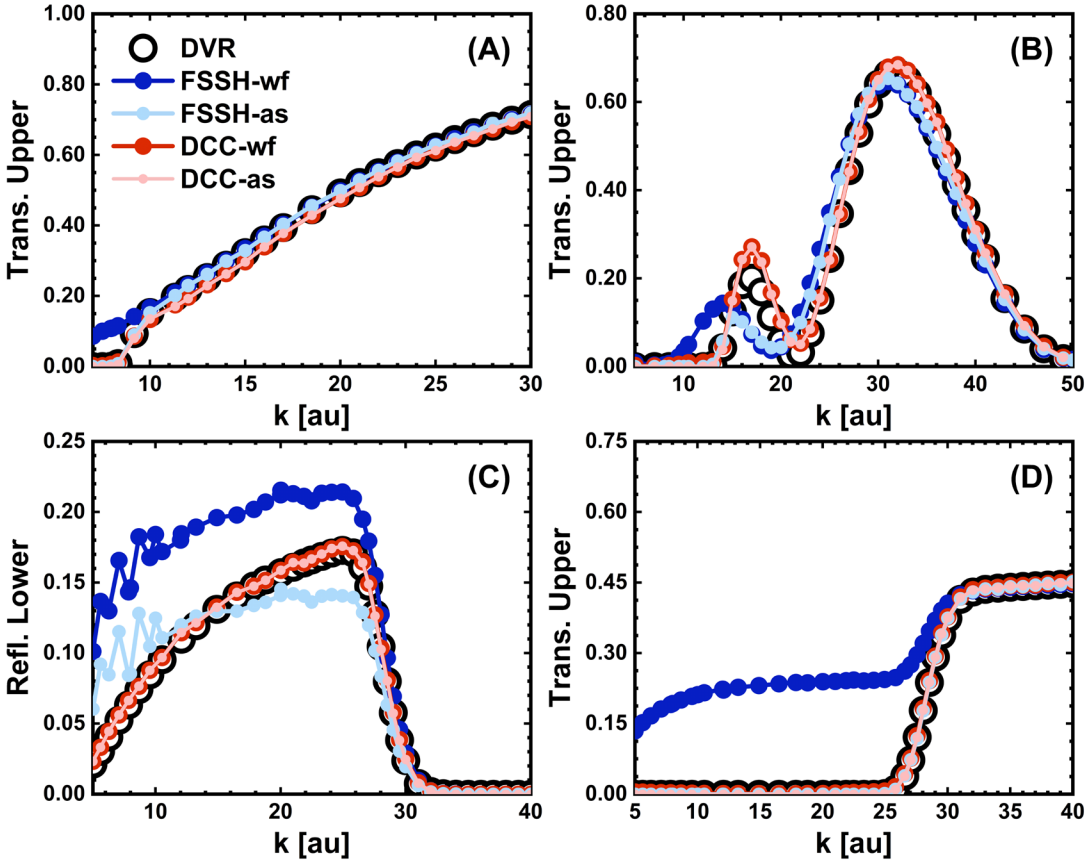

Figure 1. Transmission probabilities on the upper surface for (A) SAC and (B) DAC models, and (C) reflection probabilities on the lower surface and (D) transmission probabilities on the upper surface for the ECR model. The black open circles represent the exact quantum dynamics by DVR. The results of FSSH-wf, FSSH-as, DCC-wf and DCC-as are shown by blue, light blue, red and light red solid circles, respectively.

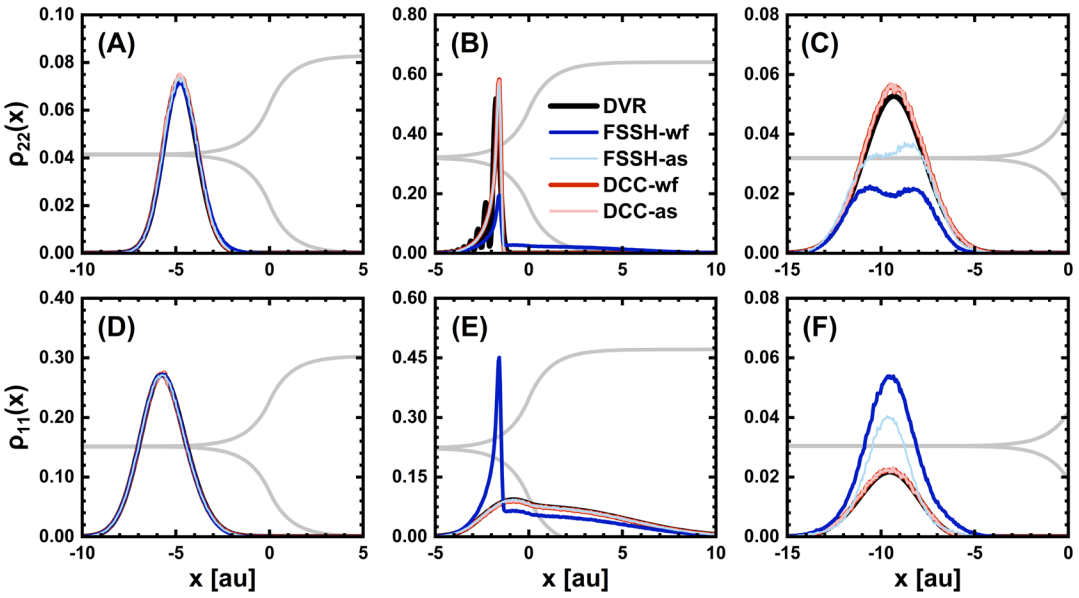

Figure 2. Population distribution on the (A-C) upper and (D-F) lower surfaces for the ECR model with the initial momentum of k = 10 au. The black lines represent the exact quantum dynamics by DVR. The results of FSSH-wf, FSSH-as, DCC-wf and DCC-as are shown by blue, light blue, red, and light red lines, respectively. The upper and lower adiabatic surfaces are shown by grey lines to guide the eyes. (A, D), (B, E) and (C, F) correspond to t = 3000, 4000 and 6000 au, respectively.

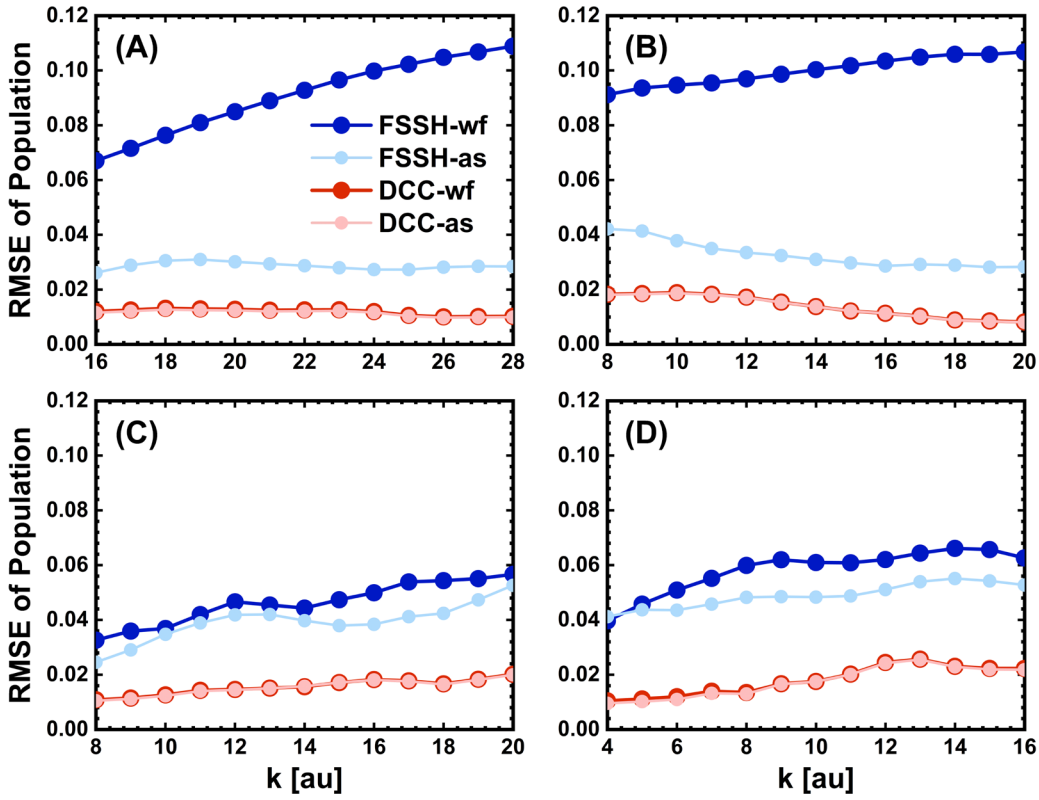

Figure 3. RMSE of population for the STD-1 model when initially starting from the (A) lower and (B) upper surfaces, and RMSE of population for the STD-2 model when initially starting from the (C) lower and (D) upper surfaces. The results of FSSH-wf, FSSH-as, DCC-wf and DCC-as are shown by blue, light blue, red and light red solid circles, respectively.

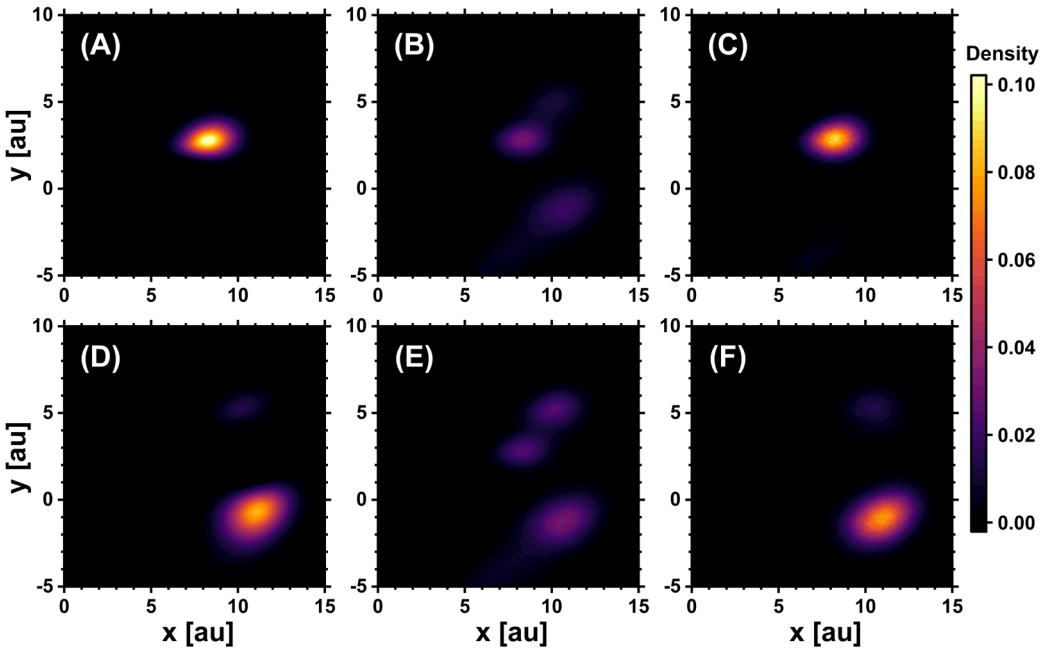

Figure 4. Spatial distribution of population for the STD-2 model on the (A-C) upper and (D-F) lower surfaces at t = 1900 au. The initial wave packet is placed on the upper surface with the parameters of x = -8, y = 0, θ = 15° and k = 16. (A, D), (B, E) and (C, F) are the results of exact quantum dynamics, FSSH-wf, and DCC-wf, respectively. The lighter colors indicate higher populations.

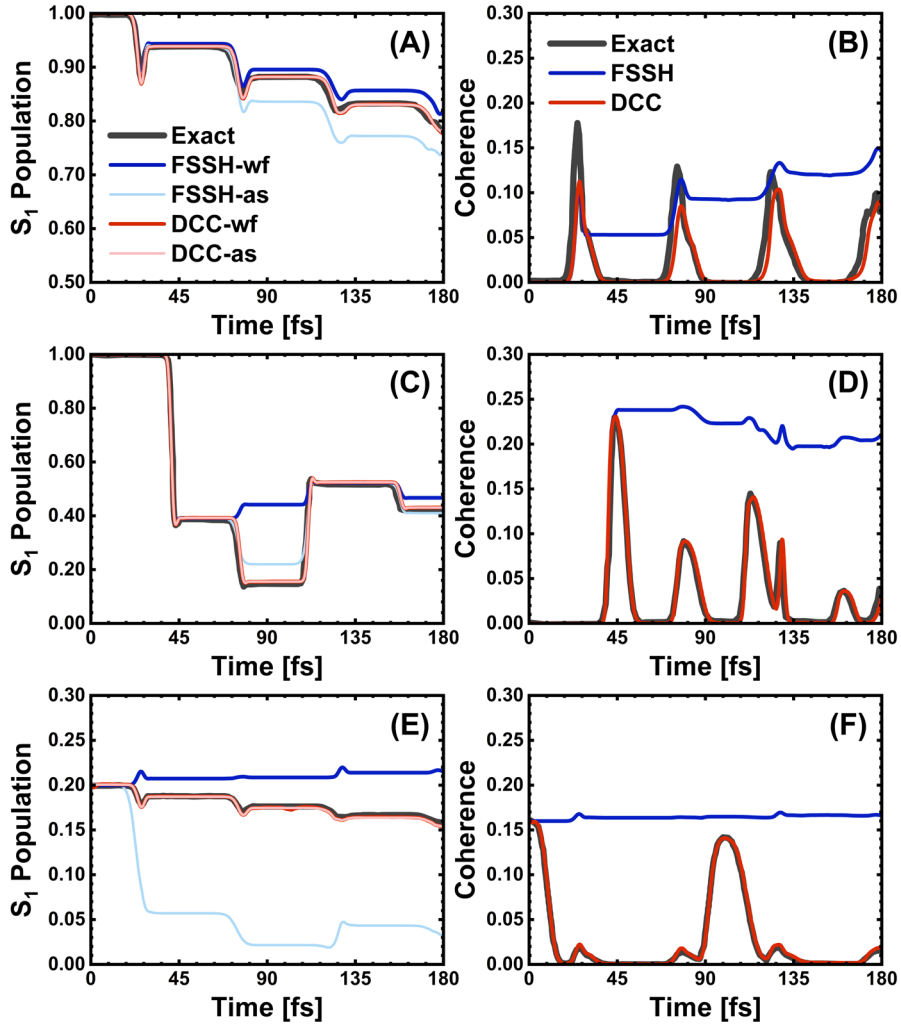

Figure 5. Time-dependent excited-state population and coherence for the (A, B) BS-1, (C, D) BS-2 and (E, F) BS-3 models. The black lines represent the exact quantum dynamics. In (A, C, E), the results of FSSH-wf, FSSH-as, DCC-wf and DCC-as are shown by blue, light blue, red and light red lines, respectively. In (B, D, F), the results of FSSH and DCC are shown by blue and red lines, respectively.

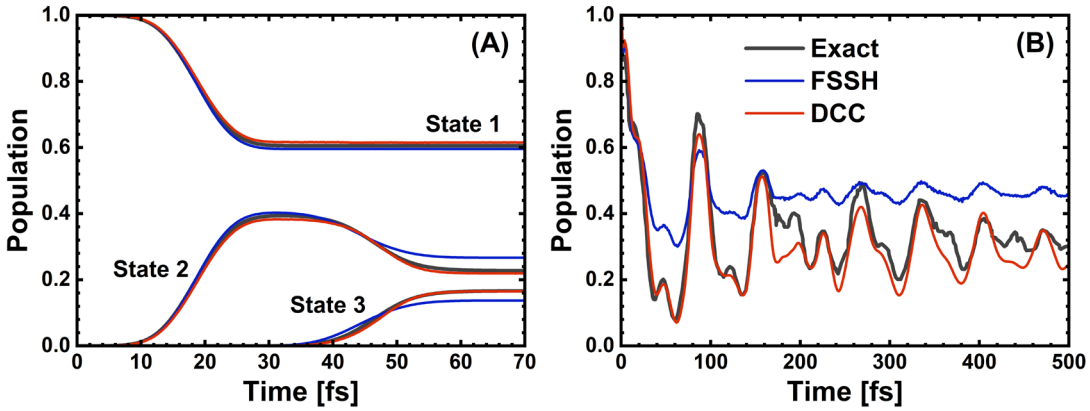

Figure 6. Time-dependent population of (A) all diabatic states for the photodissociation model and (B) diabatic state 2 for the pyrazine model. The black lines represent the exact quantum dynamics. FSSH and DCC are shown by blue and red lines, respectively.

REFERENCES

(1) Hammes-Schiffer, S.; Tully, J. C. Proton Transfer in Solution: Molecular Dynamics with Quantum Transitions. *J. Chem. Phys.* **1994**, *101*, 4657–4667.

(2) Chen, L.; Shi, Q. Quantum Rate Dynamics for Proton Transfer Reactions in Condensed Phase: The Exact Hierarchical Equations of Motion Approach. *J. Chem. Phys.* **2009**, *130*, 134505.

(3) Codescu, M.-A.; Kunze, T.; Weiß, M.; Brehm, M.; Kornilov, O.; Sebastiani, D.; Nibbering, E. T. J. Ultrafast Proton Transfer Pathways Mediated by Amphoteric Imidazole. *J. Phys. Chem. Lett.* **2023**, *14*, 4775–4785.

(4) Oberhofer, H.; Reuter, K.; Blumberger, J. Charge Transport in Molecular Materials: An Assessment of Computational Methods. *Chem. Rev.* **2017**, *117*, 10319–10357.

(5) Geng, H.; Zhu, L.; Yi, Y.; Zhu, D.; Shuai, Z. Superexchange Induced Charge Transport in Organic Donor–Acceptor Cocrystals and Copolymers: A Theoretical Perspective. *Chem. Mater.* **2019**, *31*, 6424–6434.

(6) Prodhan, S.; Qiu, J.; Ricci, M.; Roscioni, O. M.; Wang, L.; Beljonne, D. Design Rules to Maximize Charge-Carrier Mobility along Conjugated Polymer Chains. *J. Phys. Chem. Lett.* **2020**, *11*, 6519–6525.

(7) Wang, L.; Long, R.; Prezhdo, O. V. Time-Domain Ab Initio Modeling of Photoinduced Dynamics at Nanoscale Interfaces. *Annu. Rev. Phys. Chem.* **2015**, *66*, 549–579.

(8) Sneyd, A. J.; Beljonne, D.; Rao, A. A New Frontier in Exciton Transport: Transient Delocalization. *J. Phys. Chem. Lett.* **2022**, *13*, 6820–6830.

(9) Liu, J.; Zhang, X.; Lu, G. Non-Adiabatic Exciton Dynamics in van der Waals Heterostructures. *J. Phys. Chem. Lett.* **2022**, *13*, 11760–11769.

(10) Takabayashi, Y.; Sato, H.; Higashi, M. Theoretical Analysis of the Coordination-State Dependency of the Excited-State Properties and Ultrafast Relaxation Dynamics of Bacteriochlorophyll a. *Chem. Phys. Lett.* **2023**, *826*, 140669.

(11) De, P. K.; Jain, A. Metal-Induced Fast Vibrational Energy Relaxation: Quantum Nuclear Effects Captured in Diabatic Independent Electron Surface Hopping (IESH-D) Method. *J. Phys. Chem. A* **2023**, *127*, 4166–4179.

(12) Zhang, J.; Peng, J.; Zhu, Y.; Hu, D.; Lan, Z. Influence of Mode-Specific Excitation on the Nonadiabatic Dynamics of Methyl Nitrate (CH_3ONO_2). *J. Phys. Chem. Lett.* **2023**, *14*, 6542–6549.

(13) Shakiba, M.; Akimov, A. V. Machine-Learned Kohn-Sham Hamiltonian Mapping for Nonadiabatic Molecular Dynamics. *J. Chem. Theory Comput.* **2024**, *20*, 2992–3007.

(14) Zang, H.; Zhao, Y.; Liang, W. Quantum Interference in Singlet Fission: J- and H-Aggregate Behavior. *J. Phys. Chem. Lett.* **2017**, *8*, 5105–5112.

(15) Peng, J.; Hu, D.; Liu, H.; Shi, Q.; Bao, P.; Lan, Z. Studies of Nonadiabatic Dynamics in the Singlet Fission Processes of Pentacene Dimer via Tensor Network Method. *J. Chem. Phys.* **2023**, *159*, 224301.

(16) Barford, W.; Chambers, C. A. Theory of Singlet Fission in Carotenoid Dimers. *J. Chem. Phys.* **2023**, *159*, 084116.

(17) López-Carballeira, D.; Polcar, T. Singlet Fission Driven by Excited-State Intramolecular Proton Transfer (ESIPT+SF): A (TD)DFT Study. *ChemPhotoChem* **2023**, *7*, e202300017.

(18) Beck, M. H.; Jäckle, A.; Worth, G. A.; Meyer, H.-D. The Multiconfiguration Time-Dependent

Hartree (MCTDH) Method: A Highly Efficient Algorithm for Propagating Wavepackets. *Phys. Rep.* **2000**, *324*, 1–105.
(19) Wang, H.; Thoss, M. Multilayer Formulation of the Multiconfiguration Time-Dependent Hartree Theory. *J. Chem. Phys.* **2003**, *119*, 1289–1299.
(20) White, S. R. Density Matrix Formulation for Quantum Renormalization Groups. *Phys. Rev. Lett.* **1992**, 69, 2863–2866.
(21) Ren, J.; Li, W.; Jiang, T.; Wang, Y.; Shuai, Z. Time-Dependent Density Matrix Renormalization Group Method for Quantum Dynamics in Complex Systems. *Wiley Interdiscip. Rev. Comput. Mol. Sci.* **2022**, *12*, e1614.
(22) Tanimura, Y.; Kubo, R. Time Evolution of a Quantum System in Contact with a Nearly Gaussian-Markoffian Noise Bath. *J. Phys. Soc. Jpn.* **1989**, *58*, 101–114.
(23) Yan, Y.; Yang, F.; Liu, Y.; Shao, J. Hierarchical Approach Based on Stochastic Decoupling to Dissipative Systems. *Chem. Phys. Lett.* **2004**, *395*, 216–221.
(24) Xu, R.; Cui, P.; Li, X.; Mo, Y.; Yan, Y. Exact Quantum Master Equation via the Calculus on Path Integrals. *J. Chem. Phys.* **2005**, *122*, 041103.
(25) Shi, Q.; Chen, L.; Nan, G.; Xu, R.; Yan, Y. Efficient Hierarchical Liouville Space Propagator to Quantum Dissipative Dynamics. *J. Chem. Phys.* **2009**, *130*, 084105.
(26) Wang, Y.; Ke, Y.; Zhao, Y. The Hierarchical and Perturbative Forms of Stochastic Schrödinger Equations and Their Applications to Carrier Dynamics in Organic Materials. *Wiley Interdiscip. Rev. Comput. Mol. Sci.* **2019**, *9*, e1375.
(27) Kapral, R. Quantum Dynamics in Open Quantum-Classical Systems. *J. Phys.: Condens. Matter* **2015**, *27*, 073201.
(28) Wang, L.; Qiu, J.; Bai, X.; Xu, J. Surface Hopping Methods for Nonadiabatic Dynamics in Extended Systems. *Wiley Interdiscip. Rev. Comput. Mol. Sci.* **2020**, *10*, e1435.
(29) Xu, J.; Shi, Z.; Wang, L. Consistent Construction of the Density Matrix from Surface Hopping Trajectories. *J. Chem. Theory Comput.* **2024**, *20*, 2349–2361.
(30) Tully, J. C. Molecular Dynamics with Electronic Transitions. *J. Chem. Phys.* **1990**, *93*, 1061–1071.
(31) Parandekar, P. V.; Tully, J. C. Mixed Quantum-Classical Equilibrium. *J. Chem. Phys.* **2005**, *122*, 094102.
(32) Parandekar, P. V.; Tully, J. C. Detailed Balance in Ehrenfest Mixed Quantum-Classical Dynamics. *J. Chem. Theory Comput.* **2006**, *2*, 229–235.
(33) Bittner, E. R.; Rossky, P. J. Quantum Decoherence in Mixed Quantum-Classical Systems: Nonadiabatic Processes. *J. Chem. Phys.* **1995**, *103*, 8130–8143.
(34) Fang, J.-Y.; Hammes-Schiffer, S. Improvement of the Internal Consistency in Trajectory Surface Hopping. *J. Phys. Chem. A* **1999**, *103*, 9399–9407.
(35) Zhu, C.; Jasper, A. W.; Truhlar, D. G. Non-Born–Oppenheimer Trajectories with Self-Consistent Decay of Mixing. *J. Chem. Phys.* **2004**, *120*, 5543–5557.
(36) Akimov, A. V.; Prezhdo, O. V. Persistent Electronic Coherence Despite Rapid Loss of Electron-Nuclear Correlation. *J. Phys. Chem. Lett.* **2013**, *4*, 3857–3864.
(37) Subotnik, J. E.; Jain, A.; Landry, B.; Petit, A.; Ouyang, W.; Bellonzi, N. Understanding the Surface Hopping View of Electronic Transitions and Decoherence. *Annu. Rev. Phys. Chem.* **2016**, *67*, 387–417.
(38) Guo, X.; Li, G.; Shi, Z.; Wang, L. Surface Hopping with Reliable Wave Function by

Introducing Auxiliary Wave Packets to Trajectory Branching. *J. Phys. Chem. Lett.* **2024**, *15*, 3345–3353.

(39) Li, G.; Shi, Z.; Guo, X.; Wang, L. What is Missing in the Mean Field Description of Spatial Distribution of Population? Important Role of Auxiliary Wave Packets in Trajectory Branching. *J. Phys. Chem. Lett.* **2023**, *14*, 9855–9863.

(40) Landry, B. R.; Falk, M. J.; Subotnik, J. E. Communication: The Correct Interpretation of Surface Hopping Trajectories: How to Calculate Electronic Properties. *J. Chem. Phys.* **2013**, *139*, 211101.

(41) Guo, X.; Xu, J.; Li, G.; Wang, L. Interpretation of Adiabatic and Diabatic Populations from Trajectories of Branching Corrected Surface Hopping. *Chin. J. Chem. Phys.* **2022**, *35*, 488–498.

(42) Wang, L.; Trivedi, D.; Prezhdo, O. V. Global Flux Surface Hopping Approach for Mixed Quantum-Classical Dynamics. *J. Chem. Theory Comput.* **2014**, *10*, 3598–3605.

(43) Shao, C.; Xu, J.; Wang, L. Branching and Phase Corrected Surface Hopping: A Benchmark of Nonadiabatic Dynamics in Multilevel Systems. *J. Chem. Phys.* **2021**, *154*, 234109.

(44) Granucci, G.; Persico, M. Critical Appraisal of the Fewest Switches Algorithm for Surface Hopping. *J. Chem. Phys.* **2007**, *126*, 134114.

(45) Martens, C. C. Surface Hopping with Consensus. *J. Phys. Chem. Lett.* **2016**, *7*, 2610–2615.

(46) Colbert, D. T.; Miller, W. H. A Novel Discrete Variable Representation for Quantum Mechanical Reactive Scattering via the *S*-matrix Kohn Method. *J. Chem. Phys.* **1992**, *96*, 1982–1991.

(47) Manolopoulos, D. E. Derivation and Reflection Properties of a Transmission-Free Absorbing Potential. *J. Chem. Phys.* **2002**, *117*, 9552–9559.

(48) Gonzalez-Lezana, T.; Rackham, E. J.; Manolopoulos, D. E. Quantum Reactive Scattering with a Transmission-Free Absorbing Potential. *J. Chem. Phys.* **2004**, *120*, 2247–2254.

(49) Subotnik, J. E. Fewest-Switches Surface Hopping and Decoherence in Multiple Dimensions. *J. Phys. Chem. A* **2011**, *115*, 12083–12096.

(50) Shenvi, N.; Subotnik, J. E.; Yang, W. Phase-Corrected Surface Hopping: Correcting the Phase Evolution of the Electronic Wavefunction. *J. Chem. Phys.* **2011**, *135*, 024101.

(51) Pieroni, C.; Agostini, F. Nonadiabatic Dynamics with Coupled Trajectories. *J. Chem. Theory Comput.* **2021**, *17*, 5969–5991.

(52) Villaseco Arribas, E.; Maitra, N. T.; Agostini, F. Nonadiabatic Dynamics with Classical Trajectories: The Problem of an Initial Coherent Superposition of Electronic States. *J. Chem. Phys.* **2024**, *160*, 054102.

(53) Xu, J.; Wang, L. Branching Corrected Surface Hopping: Resetting Wavefunction Coefficients Based on Judgement of Wave Packet Reflection. *J. Chem. Phys.* **2019**, *150*, 164101.

(54) Coronado, E. A.; Xing, J.; Miller, W. H. Ultrafast Non-Adiabatic Dynamics of Systems with Multiple Surface Crossings: A Test of the Meyer–Miller Hamiltonian with Semiclassical Initial Value Representation Methods. *Chem. Phys. Lett.* **2001**, *349*, 521–529.

(55) Schneider, R.; Domcke, W. S_1-S_2 Conical Intersection and Ultrafast S_2-S_1 Internal Conversion in Pyrazine. *Chem. Phys. Lett.* **1988**, 150, 235-242.

(56) Zheng, J.; Xie, Y.; Jiang, S.; Long, Y.; Ning, X.; Lan, Z. Initial Sampling in Symmetrical Quasiclassical Dynamics Based on Li–Miller Mapping Hamiltonian. *Phys. Chem. Chem. Phys.* **2019**, *21*, 26502–26514.

(57) Marcus, R. A. Electron Transfer Reactions in Chemistry. Theory and Experiment. *Rev. Mod. Phys.* **1993**, *65*, 599–610.
(58) Ishizaki, A.; Fleming, G. R. Theoretical Examination of Quantum Coherence in a Photosynthetic System at Physiological Temperature. *Proc. Nat. Acad. Sci.* **2009**, *106*, 17255–17260.
(59) Caldeira, A. O.; Leggett, A. J. Quantum Tunnelling in a Dissipative System. *Ann. Phys.* **1983**, *149*, 374–456.
(60) Sun, X.; Wang, H.; Miller, W. H. Semiclassical Theory of Electronically Nonadiabatic Dynamics: Results of a Linearized Approximation to the Initial Value Representation. *J. Chem. Phys.* **1998**, *109*, 7064–7074.
(61) Wang, H.; Thoss, M.; Miller, W. H. Systematic Convergence in the Dynamical Hybrid Approach for Complex Systems: A Numerically Exact Methodology. *J. Chem. Phys.* **2001**, *115*, 2979–2990.
(62) Liu, J.; He, X.; Wu, B. Unified Formulation of Phase Space Mapping Approaches for Nonadiabatic Quantum Dynamics. *Acc. Chem. Res.* **2021**, *54*, 4215–4228.
(63) Holstein, T. Studies of Polaron Motion Part II. The "Small" Polaron. *Ann. Phys.* **1959**, *8*, 343–389.
(64) Hannewald, K.; Bobbert, P. A. *Ab Initio* Theory of Charge-Carrier Conduction in Ultrapure Organic Crystals. *Appl. Phys. Lett.* **2004**, *85*, 1535–1537.
(65) Wang, L.; Li, Q.; Shuai, Z. Effects of Pressure and Temperature on the Carrier Transports in Organic Crystal: A First-Principles Study. *J. Chem. Phys.* **2008**, *128*, 194706.